

See discussions, stats, and author profiles for this publication at: <https://www.researchgate.net/publication/244508328>

Investigation of mechanistic aspects of the catalytic CO₂ reforming of methane in a dielectric-barrier discharge using optical emission spectroscopy and kinetic modeling

ARTICLE in PHYSICAL CHEMISTRY CHEMICAL PHYSICS · FEBRUARY 2002

Impact Factor: 4.49 · DOI: 10.1039/b108040g

CITATIONS

47

READS

60

6 AUTHORS, INCLUDING:



Ken Haffner

Alstom

5 PUBLICATIONS 115 CITATIONS

[SEE PROFILE](#)



Baldur Eliasson

ABB Corporate Research, Switzerland

103 PUBLICATIONS 4,187 CITATIONS

[SEE PROFILE](#)



Ulrich Kogelschatz

ABB

118 PUBLICATIONS 6,332 CITATIONS

[SEE PROFILE](#)

Investigation of mechanistic aspects of the catalytic CO₂ reforming of methane in a dielectric-barrier discharge using optical emission spectroscopy and kinetic modeling

Martin Kraus,^{*a} Walter Egli,^d Ken Haffner,^c Baldur Eliasson,^b Ulrich Kogelschatz^b and Alexander Wokaun^a

^a Paul Scherrer Institute, 5232, Villigen PSI, Switzerland. E-mail: martin.kraus@gmx.net

^b ABB Corporate Research Ltd., 5405, Baden, Switzerland

^c Alstom Power Technology, 5405, Baden, Switzerland

^d Alte Bettswiler Str. 7a, 8344, Bäretswil, Switzerland

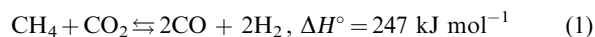
Received 5th September 2001, Accepted 5th December 2001

First published as an Advance Article on the web 16th January 2002

The CO₂ reforming of methane by the combination of catalysts with a dielectric-barrier discharge is investigated as an alternative approach to the conventional pure catalytic process. It is shown that the use of nickel or calcium-promoted nickel catalysts in combination with the discharge leads to an increase in the CO yield of 20 to 40%. The identified products are CO, H₂, water, ethane and ethylene, propane, n-butane and methanol. In addition to the experimental investigation, extensive kinetic modeling was performed. Besides a good description of the plasma reactions by a set of 308 reactions and 57 species, the programs used offered the possibility of identifying the main reaction routes towards the different products. To get an insight into the mechanistic aspects of the catalyst–plasma interaction, the gas phase was investigated with optical emission spectroscopy (OES) during the experiment. Special emphasis was placed on the interpretation of differences in the emission spectra from experiments with and without a catalyst in the discharge. A significant difference was observed for the CH A ²Δ–X ²Π band. Therein, the intensity of the signal was proportional to the activity of the catalysts used, in the sense that the CH signal was higher for a more active catalyst. Based on these results, a tentative reaction scheme is proposed that explains the enhancing effects of the catalysts in the CO₂ reforming reaction. It starts with the adsorption of methane and methane fragments from the gas phase, followed by their gasification by oxygen and oxygen-containing species supplied by the discharge plasma.

Introduction

The conversion of methane to products like synthesis gas (CO/H₂), liquid fuels or basic chemicals is a basis of modern chemical industry. Since methane itself is an extremely stable molecule that is not easy to activate for a reaction, a major part of the processes dealing with methane conversion is based on reaction steps which use solid oxide or metal catalysts. These catalysts enable the reactions to proceed at lower temperatures and with increased speed. However, some of the processes, like for example the conversion of methane with carbon dioxide to synthesis gas (see eqn. (1)), still require extreme reaction conditions with high temperatures and pressures (typically up to 1000 °C at 40 bar).



It is therefore still of major interest in catalyst research to evaluate the possibilities to perform such processes under milder conditions and with higher product yields. A possible approach to this problem was presented by Eliasson *et al.*¹ in 1998. In their studies of the catalytic methanol synthesis from carbon dioxide and hydrogen they showed that combination of the conventional catalyst with a dielectric-barrier discharge could enhance the activity of the catalyst and lower the temperature needed for optimum yield. The dielectric-barrier discharge (DBD) is today in widespread use for industrial ozone production, which is used for water and air treatment.² In

addition, many new DBD applications exist today, such as CO₂ lasers, excimer lamps or plasma display panels.^{3,4} The specific properties of this discharge are especially suited for the initiation of plasma chemical processes, since the electrons generated in DBDs have mean energies in the range 1 to 10 eV.⁵ The second important aspect is the possibility of producing a plasma at atmospheric pressure and above without having the extremely high temperatures present in an electric arc. The key for the functioning of the dielectric-barrier discharge is the presence of at least one dielectric in the discharge gap. The dielectric serves two functions in the system. First, when local breakdown occurs, it terminates the current flow through the discharge gap at that specific location after a few nanoseconds. Secondly, the resulting microdischarges in the discharge gap with a radius of only 0.1 mm are distributed over the whole electrode area.

The principle of combining a dielectric-barrier discharge with a heterogeneous catalyst has now been applied to the above-mentioned reaction of CH₄ with CO₂, the so-called CO₂ reforming of methane. The idea was that if it were possible to activate the reactants in the discharge prior to the catalytic reaction, then this should have a positive influence on the reaction conditions.

In our last paper,⁶ we already presented some results from combined experiments with different catalysts in the discharge for CH₄ and CO₂ decomposition alone (each gas fed separately) and in the CO₂ reforming of methane. These investigations included a nickel, a calcium-promoted nickel and a

rhodium-coated catalyst. Regarding the nickel-based catalysts, an increase in the activity was observed for the CO₂ reforming of methane, while the product yields remained nearly unchanged for the methane decomposition and were found to be lower for the CO₂ decomposition, compared to the pure gas discharge without catalyst. Furthermore, the rhodium-coated catalyst led in all cases to lower conversion than with the gas discharge. Since the best results were achieved with the nickel-based catalysts, we focus in the present investigation on the CO₂ reforming reaction with nickel-based catalysts and DBD. To obtain a better understanding of the plasma-catalyst interaction, we implemented diagnostics for optical emission spectroscopy and performed numerical kinetic modeling of the discharge processes. Furthermore, we modified the catalytic DBD reactor for use at higher temperatures. The results are presented below.

Experimental

Reactor and high voltage driving circuit

The catalytic DBD reactor system was already described in detail in ref. 6. The reactor consists of an outer quartz tube with an outer diameter of 33 mm and a wall thickness of 1.5 mm. The inner tube has an outer diameter of 18 mm, resulting in a radial discharge gap width of 6 mm. A steel foil wrapped around the outer tube serves as the ground electrode. The alternating high voltage is supplied to the inner wall of the inner tube by a metal spring. The ceramic foam catalyst is placed in the annular discharge gap between the two quartz tubes. To fill voids between the catalysts and the walls, a thin layer of quartz wool surrounded the catalysts. The reactor was heated with a recirculating oil flow from a thermostat. As an improvement over the reactor system described in ref. 6, the fittings of the reactor were replaced by newly designed aluminium fittings with Kalrez® (DuPont) O-rings, which allowed an increase in the maximum operating temperature from 230 °C to 300 °C.

The gases are supplied to the reactor through digital mass flow controllers (Bronkhorst EL-Flow, The Netherlands). To quantify the total gas flow at the outlet of the reactor and to monitor volume changes during the reaction, a small amount of nitrogen is added to the reaction gas behind the reactor with a separate digital mass flow controller. The mass flow controllers are controlled with a LabVIEW™ 5.0 (National Instruments) Macro based on the Flowbus™ software from Bronkhorst, The Netherlands. The product gases are analyzed with a micro gas chromatograph (Hewlett-Packard M 200 H). It is equipped with two columns, a 10 m molecular sieve column (for the detection of H₂, N₂, O₂, CH₄ and CO) and an 8 m Poraplot Q column (for the detection of CO₂, H₂O and hydrocarbons). Both columns are used with thermal conductivity detectors (TCDs). Helium 5.0 (Sauerstoffwerke Lenzburg, Switzerland) is used as the carrier gas for the gas chromatograph (GC). The GC was calibrated by using reference gas mixtures from Sauerstoffwerk Lenzburg, Switzerland and Messer Griesheim, Switzerland. The analysis was performed isothermally at 100 °C for the molecular sieve column and 120 °C for the Poraplot Q column. The run time for one analysis was 125 s for experiments without hydrocarbon formation and 160 s, if hydrocarbons were present. Since the hydrogen peak was overlaid by hydrocarbon peaks having the same retention time on the GC, the reaction gases were passed through a column filled with active carbon where the hydrocarbons were removed. For hydrocarbon detection, this column was bypassed. The C₂ hydrocarbons ethane and ethylene were not separated during the analysis and appeared therefore at the same retention time as one peak. For calibration, a similar response of ethane and ethylene on the TCD was

assumed. Hydrocarbons higher than C₄ were not measurable on the Micro GC. Water was calibrated with a one-point calibration, using the partial pressure in the laboratory air. A linear response over the detected concentration range was assumed. All gas lines from the reactor to the analysis system were heated to 90 °C by silicon rubber tubes connected to a recirculating hot water flow to avoid condensation of products.

High voltage circuit

To drive the discharge, a high voltage pulser (Fraunhofer Institute for Laser Technology, Aachen, Germany) was used. It generates high voltage pulses with a maximum amplitude of 20 kV and a half width of approximately 2 μs. The pulse repetition rate was 13.8 kHz. The method of power determination from voltage charge Lissajous figures was already described in ref. 6 and was originally proposed by Manley.⁷ The high voltage signals are measured with a HV probe (LeCroy PPE 20 kV). The charge is determined with a Q-probe (measuring capacitance with negligible inductivity) with a capacitance of 314 nF. The signals are displayed on a digital scope (LeCroy LC 574 AM) having a maximum sampling rate of one gigasample s⁻¹. The electric power in the experiments performed was 10.5 W. The power density (power per electrode area) PF^{-1} was calculated for an average electrode area, since inner and outer electrode were of different sizes. It amounts to 14 kW m⁻².

UV/VIS spectrometer specifications and configuration

The spectrometer system was obtained from Ocean Optics Inc., Florida (U.S.). It consists of two miniature fiber optic spectrometers AVS-2000 connected *via* a bus system. The spectrometers use asymmetric crossed Czerny–Turner configurations with focal lengths of 42 mm. Holographic gratings with 1800 lines mm⁻¹ and a usable wavelength range 200–635 nm were used. The width of the entrance slit was 50 μm. The wavelength range for the two spectrometers was from 250 to 400 and from 400 to 570 nm, respectively. The detectors used were 2048-element linear CCD array detectors (Sony ILX511 CCD) with a special upgrade for improved UV sensitivity. To reduce the statistical noise of the detectors, the spectrometers were cooled to -10 °C. The optical fibers used were 600 μm multi-mode silica fibers, optimized for use in the UV–VIS region. Each spectrometer was equipped with a separate fiber. The optical resolution, given as the full width at half maximum (FWHM), was determined using a low pressure Hg–Ar lamp (Oriol pen-ray, Oriol Inc., CT, USA) and the mercury line at 435.833 nm and found to be 1.34 nm. The spectral response of the spectrometers with attached fibers was determined using a deuterium lamp for the UV region and a black body cavity (SIKA Electronic) for the VIS region. The acquisition time for the emission spectra was 40 s, due to the low light emission from the discharge.

The optical fibers were placed in the discharge gap in front of or behind the active plasma zone at approximately 5 mm distance to avoid destruction of the fiber and material deposition on the polished fiber tip.

Catalysts

The active nickel and nickel–calcium layer was supported on ceramic foams with 92% alumina and 8% silica and a porosity of 45 pores per inch (ppi) (Vesuvius Hi-Tec Ceramics, New York). The foams had the shape of hollow cylinders of length 10 mm, inner diameter 18 mm and outer diameter 30 mm. To increase the specific surface area of the foams, they were already delivered from the manufacturer with an alumina washcoat.

Table 1 Catalyst compositions

Catalyst	Composition (wt.%)	Surface area (liq. N ₂ BET)/ m ² g ⁻¹
Raw foam	92% Al ₂ O ₃ , 8% SiO ₂ Alumina washcoat	11.0
Nickel/ calcium-coated foam	Support: same as above Coating: 2.6% Ni 1.8% Ca	7.5
Nickel-coated foam	Support: same as above Coating: 6% Ni	10.6

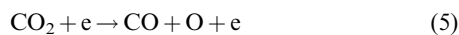
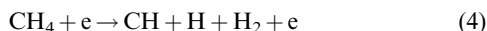
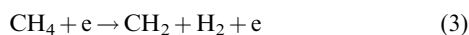
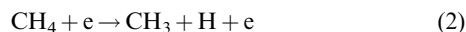
The impregnation process for the catalysts was described in a previous paper.⁶ The measured BET surface area of the foam catalysts and their composition are shown in Table 1.

Before performing experiments, the nickel catalysts were reduced in a gas flow of 200 ml_n min⁻¹ nitrogen and 30 ml_n min⁻¹ hydrogen (where ml_n = normal milliliters, standard conditions), resulting in a space velocity of 2700 h⁻¹. All gases used in the experiments were supplied by Sauerstoffwerke Lenzburg, Switzerland with a purity of 99.99% (CO₂), and 99.995% (CH₄ and H₂), respectively. Nitrogen was supplied from the laboratory gas line connected to a liquid N₂ container.

The catalysts for the experiments with discharge and catalysts were tested between 40 and 300 °C at a space velocity of 1300 h⁻¹ in a gas mixture of 75% CO₂ and 25% CH₄. The low space velocity that is unusual for pure catalytic experiments was chosen to obtain sufficiently high conversion in the short discharge section.

Numerical simulation of gas phase reactions

The details of the kinetic model and the modeling of the silent discharge itself are found in ref. 8–11. The microdischarges are regarded as a source of electrons that dissociate molecules in the gas phase according to the plasmachemical reactions:



with reaction rates a , b , c and d . Assuming that the electron density varies much faster than other species concentrations in the discharge, the corresponding electronic equations for eqn. (2)–(5) can be integrated (see ref. 10). As a result, we obtain the density of radicals, fragments and molecules generated in each microdischarge:

$$[\text{CH}_3] = \alpha[\text{CH}_4] \quad (6)$$

$$[\text{CH}_2] = \beta[\text{CH}_4] \quad (7)$$

$$[\text{CH}] = \gamma[\text{CH}_4] \quad (8)$$

$$[\text{O}] = [\text{CO}] = \delta[\text{CO}_2] \quad (9)$$

$$[\text{H}] = (\alpha + \gamma)[\text{CH}_4] \quad (10)$$

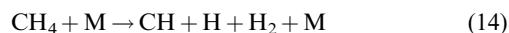
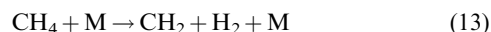
$$[\text{H}_2] = (\beta + \gamma)[\text{CH}_4] \quad (11)$$

with the coefficients α , β , γ and δ as functions of the electron density generated by one microdischarge pulse and the corresponding rate coefficients of eqn. (2)–(5). The values

of the coefficients α , β , γ and δ depend on plasma parameters such as electron energy, gas composition, gap width, *etc.* In the present investigation they were determined by fitting the computed yields of stable products to the measurements.

[CH₃], [CH₂], [CH], [H], [O] and [CO] are the initial radical and molecule concentrations for the chemical reactions taking place after the first microdischarge at time $t = 0$. Usually the model includes more than one discharge pulse, which makes it necessary to sum the densities of previous pulses at the starting time of each pulse.

Although this pulsewise discharge model delivered good results for most of the calculations performed, it was not very well suited for very large reactions systems with many species and a high number of pulses. In such a case, the computation time was extremely long. Therefore, the model was simplified to speed up the calculations. The pulsewise model was converted into a continuous model. The principle will be explained with the four decomposition reactions shown above. The corresponding “thermal” reactions analogous to eqn. (2)–(5) are:



It is clear that the reaction rates for the three steps are negligibly small in the temperature range 40–300 °C. To include now the radical production from the discharge processes in the thermal rates, an extra term is added to the thermal dissociation rate:

$$\rho_{\text{eff}} = \rho_{\text{thermal}} + \rho_{\text{dis}} \quad \text{with} \quad \rho_{\text{dis}} = \frac{N\alpha}{2\tau[\text{M}]} \quad (16)$$

where ρ_{eff} is the effective rate, ρ_{thermal} is the rate of the pure thermal process, N is the total number of pulses and τ is the time during which the gas is affected by the plasma. This simple model does not consider changes in electrical parameters of the discharge with temperature, pressure, *etc.* Furthermore, no charged particles are included in the data set, but only radical reactions are considered.

The full reaction system that was used for the simulation contained 308 reactions and is found in ref. 12. The following 57 species were included in the calculations:

O, CO, CO₂, H, H₂, O₂, O₃, HCO, HO₂, CH₂, OH, H₂O, H₂O₂, C₂, CH₃, CH₄, CH₂O, CH₃O, CH, CH₃O₂, CH₂OH, CH₃OH, CH₃OOH, C₂H₆O, C₂H₅O, C₂H₆, C₂H₄, C₂H₅, C₂H, C₂H₂, C₂H₃, CH₃CO, CH₃CHO, i-C₃H₇, C₃H₈, n-C₃H₇, C₄H₇, C₄H₈, C₃H₅, C₃H₆, n-C₄H₁₀, i-C₄H₁₀, i-C₄H₉, t-C₄H₉, n-C₄H₉, C₄H₉O, C₄H₉OH, i-C₅H₁₂, n-C₅H₁₂, CH₂CHO, CH₂CO, C₅H₁₀, C₅H₁₁, HCCO, HOCHCH, C₅H₉, C.

The numerical solution of this reaction system is done in two steps with the help of the program KINETICS.¹³ First, the chemical kinetic system is transformed into a stiff system of ordinary differential equations. This step is done automatically in an interpreter mode. The second step is to solve and integrate numerically the system of differential equations. In this case we used the stiff ODE solver METAN1.¹⁴

To keep the system as small as possible, hydrocarbons larger than C₄ were only included in the reaction system if it appeared necessary for the result. All reactions were extracted from NIST chemical reference database #17.¹⁵ Whenever possible, the rate data were taken from Tsang *et al.*,^{16–20} a source which provided by far the most complete set of data.

Analysis of the important reaction pathways

To isolate the important reaction pathways from the pool of reactions a second program has been developed. The complete concept of the program has been described in detail in ref. 12.

The reaction scheme is regarded as an oriented bipartite graph, where the knots are the species concentrations and the reactions, as shown in Fig. 1(a).

The lines (edges) of the graph are the connection between the two subsets of nodes S and R and represent the flux of the species “over” a certain reaction (the “chemical conversion” of a species caused by a certain reaction). The time derivative of a species concentration S_i is equal to the sum of contributions from all reactions in the system.

$$\dot{S}_i = \sum_k \dot{y}_{ik} \quad (17)$$

with y_{ik} as the positive or negative contribution of the reaction k to the concentration of S_i . The integral of this reaction contribution over the total reaction time gives the mass flux f_{ik} “through” the reaction k during reaction time τ .

$$f_{ik} = \frac{1}{\tau} \int_{t=0}^{t=\tau} \dot{y}_{ik} dt \quad (18)$$

The lines between two species S_i and S_k are now given a length by weighting with the inverse mass flux w_{ik} .

$$w_{ik} = \frac{1}{|f_{ik}|} \quad (19)$$

The weighting coefficients w_{ik} , with respect to the flux values f_{ik} , can be found by using eqn. (17)–(19). It is useful to implement these calculations in the integration process of the kinetic system described before. Depending on whether the decrease or the increase of a species is investigated, the program identifies the corresponding shortest (*i.e.* fastest) pathways from one species to the other species in the reaction system in the order of importance, as shown in Fig. 1(b).

Results

Influence of the catalyst on the product yield

Although the temperature range has now been extended from 230 to 300 °C, the yields obtained for CO as the main product

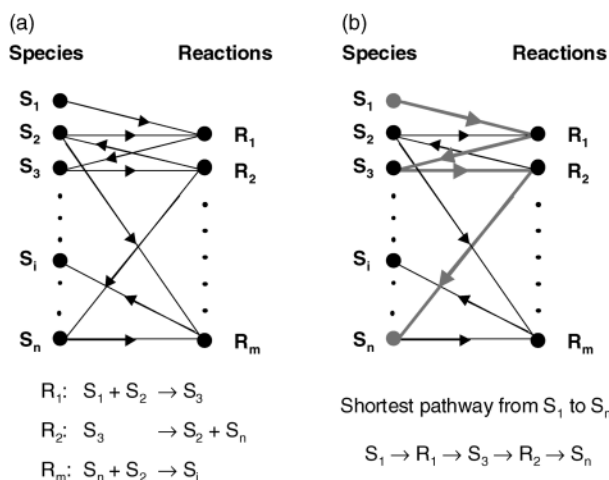


Fig. 1 (a) Presentation of a reaction scheme as a directed bipartite graph, (b) shortest pathway as the result of the calculation (bold arrows).

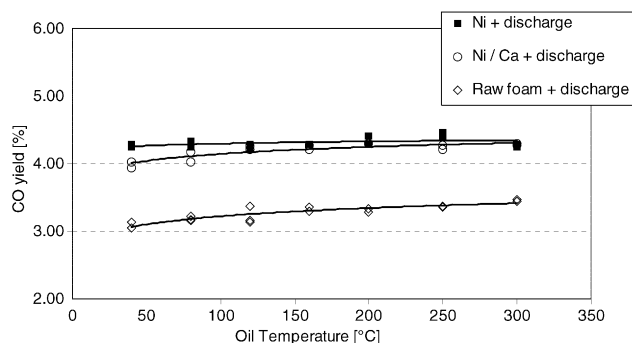


Fig. 2 CO yield from CO₂ reforming of methane, comparison of uncoated and metal-coated alumina foams in the discharge.

followed the former results (Fig. 2).⁶ Without the discharge, no conversion was observed in the investigated temperature range. This is in agreement with equilibrium calculations that were performed on the basis of the set oil temperatures (calculated equilibrium yield of CO at 300 °C only 0.9%). The use of a nickel or a calcium-promoted nickel catalyst in combination with the discharge led to a significant increase in the CO yield, compared to the use of an uncoated alumina foam in the discharge. While the yield in the case of the uncoated foam was in the range 3 to 3.5%, the presence of nickel in the discharge gap resulted in values that were between 20 and 40% higher. As was also explained in our last paper, the addition of calcium to the nickel catalyst did not significantly change the activity of the catalyst in the discharge towards the products. Although the positive influence of the nickel catalyst was similar to that of our former results, the temperature dependence was much less pronounced in the modified reactor. The most likely explanation is an unwanted corona discharge at the metal fittings (before the modification, plastic fittings had been used) and a resulting wrong determination of electrical input power. Since such an additional power loss would be more pronounced with increasing temperature, it could explain the observation. Unfortunately, this problem remains unsolved.

In addition to the results that were presented in our recent paper for the CO₂ reforming of methane with discharge and catalyst,⁶ an analysis of the hydrocarbons produced was implemented. Besides the products H₂, CO and water, the detected hydrocarbons and oxygenates were (in order of amount) ethane/ethylene, propane, methanol and n-butane. In contrast to the production of CO and H₂, the concentrations of these hydrocarbons in the product gas were hardly changed by the presence of a nickel catalyst in the discharge. Therefore, only a typical analysis is shown in Fig. 3 for an uncoated alumina foam without comparison with the nickel catalysts. Since ethane (C₂H₆) and ethylene (C₂H₄) were not separated

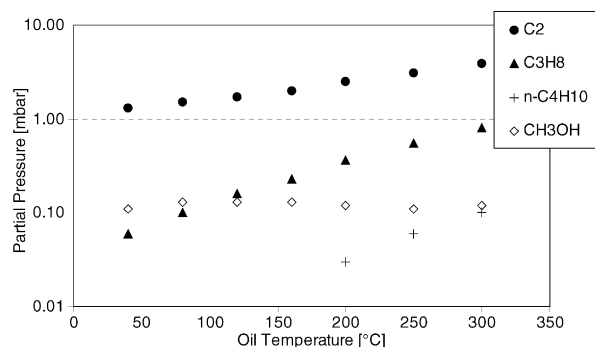


Fig. 3 Measured hydrocarbon concentrations in CO₂ reforming of methane with an uncoated foam in the discharge, species as indicated in the legend.

on the GC column used, they are shown together as “C₂”. Although no separation of these two components was achieved, former analyses on a conventional gas chromatograph showed that a discharge in methane-containing gas mixtures always produces a mixture of both components. The amount of C₂H₆/C₂H₄ showed an increase from 1 mbar at 40 °C to 4 mbar at 300 °C. The propane concentration was at the same time rising much faster, ranging from less than 0.1 mbar at 40 °C to nearly 1 mbar at the highest temperature. The amount of methanol stayed nearly constant at 0.1 mbar, while n-butane was only present between 200 °C and 300 °C with concentrations rising from near zero to 0.1 mbar.

No other significant amounts of hydrocarbons were measured in this mixture. Some traces of other oxygenated species were detected. However, they could not be identified, although several components like acetone, ethanol, formaldehyde *etc.* were tested on the GC.

Since the real surface reactions in the combined plasma–catalyst experiments were not accessible with our present set-up, we tried to explain the observation that the presence of nickel in the DBD had a positive influence on the product yield in the CO₂ reforming of methane by other approaches. The first step was a numeric modeling of the gas phase reactions in the plasma. This investigation was done to get an idea of the radical chemistry in the gas and, using the result of this modeling, to deduce possible mechanisms for the gas phase–surface interaction. The results of the modeling are shown in the next section. Secondly, spectroscopic investigations of the gas phase were performed to identify single plasma species and extract eventual differences between experiments with and without a catalyst in the discharge. The results of the spectroscopic investigations are presented in the section after the modeling.

Modeling of the discharge gas phase reactions in CO₂ reforming of methane

The CO₂ reforming reaction was simulated by varying the dissociation rates $\rho_{\text{dis}}(\alpha)$, $\rho_{\text{dis}}(\beta)$, $\rho_{\text{dis}}(\gamma)$ and $\rho_{\text{dis}}(\delta)$ to obtain a suitable fit at 40 °C, as described in the theoretical part. The determined coefficients α , β , γ , δ were then kept constant at all temperatures. The best fit of the simulation to the experimental data (at 40 °C) was obtained for:

$$\rho_{\text{dis}}(\alpha) = 1.0 \times 10^{-3} \text{ s}^{-1} \quad (20)$$

$$\rho_{\text{dis}}(\beta) = 1.4 \times 10^{-2} \text{ s}^{-1} \quad (21)$$

$$\rho_{\text{dis}}(\gamma) = 5.0 \times 10^{-4} \text{ s}^{-1} \quad (22)$$

$$\rho_{\text{dis}}(\delta) = 1.1 \times 10^{-2} \text{ s}^{-1} \quad (23)$$

The modeling results are shown in Fig. 4.

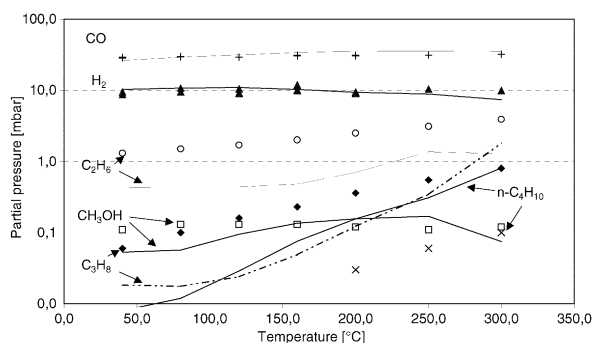


Fig. 4 CO₂ reforming of methane, product partial pressures, lines are the result from simulation. Points are the values obtained from an experiment with uncoated ceramic foam.

A good agreement over the whole temperature range was found for the main products hydrogen and carbon monoxide. In addition, the ethane and methanol showed a reasonable agreement with the experimental data, although the ethane values obtained from the modeling were slightly too low. The partial pressure of propane was also lower compared to the experiments and showed a strong increase with temperature. In contrast, the values obtained for n-butane were higher than found in the experiment and also rising too fast with temperature. The discrepancies for propane and butane are probably related to an insufficient data set for the two hydrocarbons that lead to a wrong temperature dependence. The water value that was found with the model was higher than in the experiment and rose strongly with temperature (9 to 18 mbar). However, regarding the limitations of the model, the overall agreement was much better than could have been expected. Besides the components that were found in the experiment by gas chromatography, small partial pressures of other molecules were present in the modeling result. There were mainly three components with considerable partial pressure, formaldehyde (10^{-1} mbar), ethylene (10^{-3} to 10^{-1} mbar) and isobutane (10^{-2} mbar). All other components had significantly lower partial pressures. Assuming the correctness of the model, the measured partial pressures indicated in Fig. 3 as C₂ (C₂H₆/C₂H₄) were probably mostly ethane.

For the products measured in the experiments, an analysis of the main reaction pathways according to the model presented in the theoretical section was performed. Hydrogen was not included in this investigation, since the three initial methane decomposition reactions (eqn. (2)–(4)) with their modified reaction rates had the highest influence on the hydrogen yield.

Fig. 5 shows the pathway analysis for the hydrocarbons. Two reaction pathways to ethane/ethylene, propane and n-butane were identified to have an important influence on the product yield. The first starts from the CH₃ radical, leading to the formation of ethane and the higher homologous hydrocarbons propane and butane. This mechanism proceeds *via* the addition of CH₂ units to the hydrocarbons. The second pathway, which had a higher impact on the product yield, starts with the formation of ethylene from methane and CH. The next step is the formation of a C₂H₅ radical, which then reacts further, to butane by the addition of a second C₂H₅ radical or to ethane by the addition of a hydrogen atom. The formation of propane is similar in both pathways, although a reaction of C₂H₅ with CH₃ would be an alternative reaction path that was implemented in the simulation code.

In a second step, the reaction pathways to methanol and CO were investigated. The reaction scheme is shown in Fig. 6.

The reaction path to methanol includes a few steps from CO₂ over formaldehyde and several intermediates. Although it was not found in the gas chromatograph analysis,

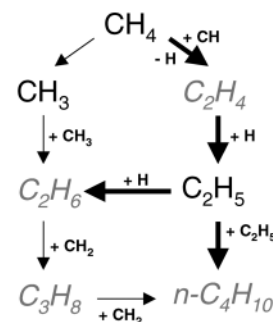


Fig. 5 Main reaction pathways in the CO₂ reforming of methane to the observed hydrocarbons from the experiments, products indicated in italic and gray, intermediates in black, the main pathway is indicated with bold arrows.

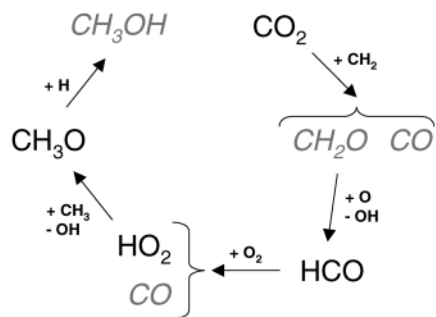


Fig. 6 Main reaction pathways in CO₂ reforming of methane to methanol, CO and formaldehyde, products indicated in gray and italic, intermediates in black.

formaldehyde seems to be an important intermediate towards methanol formation and, as mentioned above, was also present as a product in the modeling result with a similar partial pressure to that of methanol.

Besides the direct decomposition of CO₂, two other similarly important pathways for CO production could be identified, as shown in Fig. 6. The first was the co-generation of CO during formaldehyde formation, while additional CO originated from the reaction of the HCO radical with molecular oxygen.

Identification of discharge species

As a second step towards a better understanding of the processes in the discharge, the gas phase in the discharge was investigated with optical emission spectroscopy during the experiments. The idea was to identify and isolate differences in the spectra originating from catalyst and non-catalyst experiments. The spectra were acquired with the Ocean Optics spectrometer system that has already been described in the experimental section. The optical fibers were positioned inside the discharge gap close to the reactor wall approximately 5 mm in front of the discharge zone. For some experiments, the fibers were placed behind the discharge zone to monitor possible changes in species concentration. The identification of discharge species was done with the help of the book by Pearse and Gaydon.²¹

All peaks in the spectrum between 250 and 400 nm were normalized with respect to the highest peak of the CO₂ band system between 300 and 400 nm. This was necessary, since comparison between different spectra showed that normalization to the overall highest peak led to large differences in the baseline levels. Furthermore, such normalization made sense, since, due to the high concentration of CO₂, the carbon dioxide peaks could be regarded as a “background” signal that was independent of product concentrations. The acquired spectra are shown in Fig. 7 and 8.

Identification of single emission bands was only attempted for clearly separated peaks. Most of the complex spectrum of carbon dioxide was not assigned to single species, which was due to the low resolution of the spectrometers and the lack of reference data.

These unassigned peaks are indicated in Fig. 7 as “CO₂” in the spectrum. The major emission bands of CO₂ are found in the region between 290 and 400 nm, as shown in Fig. 7. Besides the typical strong band system above 300 nm, some single bands were identified.

At 283 and 297 nm, two bands of the third positive system of carbon monoxide were found, which are typical of CO-containing discharges. In between these two emission peaks, a strong double-band of CO₂⁺ appears in the spectrum. At 306 nm, the OH A²Σ⁺–X²Π system appeared, which was found to be extremely weak compared to its usual strength for example in flames and water vapor-containing discharges. Since the OH radicals can be regarded as a precursor of water, the weak

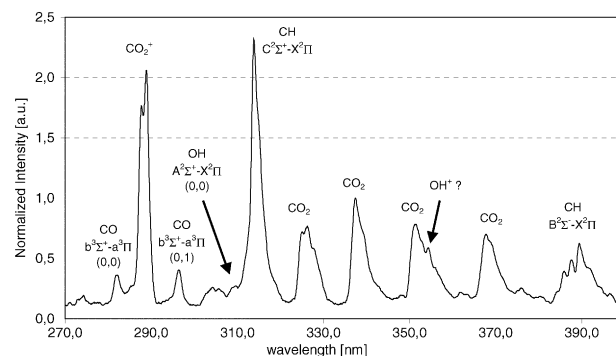


Fig. 7 Emission spectrum recording during CO₂ reforming, gas discharge, 250–400 nm, 40 °C.

emission from OH agrees well with the low water contents found in the product gas by gas chromatography.

The highest peak below 400 nm was found to be the CH C²Σ–X²Π system at 314 nm, which is ascribed to the C²Σ–X²Π (1,1) and (0,0) transitions. This band was extremely intense, compared to its occurrence in flames, for example. At 356 nm, a small spike on the shoulder of a CO₂ band appeared. It was not assigned in the spectrum shown above, but it might belong to the OH⁺ ³Π–³Σ (0,0) transition. The peak at 390 nm belongs to the CH B²Σ–X²Π transition. According to the reference file, the signal should be mainly caused by the (0,0) transition, since the intensity of the other transitions is usually very low.

At higher wavelengths, between 390 and 570 nm, the spectrum was dominated by the CH A²Δ–X²Π system between 420 and 440 nm, as shown in Fig. 8. It consists of four main transitions, which are CH A²Δ–X²Π (0,0) up to (3,3). Besides the CO₂ bands at 412 and 435 nm, three bands from CO at 483, 520 and 561 nm could be identified, which belong to the Ångström system. The last three peaks in the spectrum at 512, 516 and 558 were part of the C₂ Swan system. The C₂ species are formed during degradation of hydrocarbons in the discharge and are therefore regarded as a step towards carbon formation. However, despite the long acquisition time, most of the peaks above the wavelength range of the CH A²Δ–X²Π signals were often hardly more than noise on the baseline.

Comparative analysis of emission spectra

Subsequent to the identification of the plasma species, the emission spectra from different experiments with and without catalysts were compared to identify conceivable differences. In addition to the spectra obtained at the inlet side of the reaction zone, the optical fibers were placed at the outlet side for comparison. For most of the peaks observed, the differences

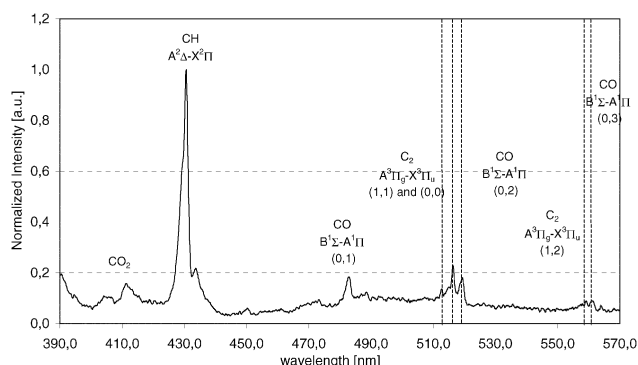


Fig. 8 Emission spectrum recording during CO₂ reforming, gas discharge, 390–570 nm, 40 °C.

were in the range of experimental error and therefore negligible. Since no significant changes in emission were observed above 400 nm with different catalysts, the analysis was limited to the lower wavelength range.

Differences in emission strength were mainly observed for 4 peaks, the two CO peaks at 283 and 297 nm, the double band of CO_2^+ at 288/289 nm and the CH C-X band at 314 nm. The CO_2^+ signal was excluded from the discussion, since no clear trend could be extracted from the spectra.

As a first step, the two CO signals at 283 and 297 nm from different experiments with and without a catalyst in the discharge were compared. Examples of the emission from an experiment with a nickel-coated and a raw foam are shown in Fig. 9 and 10.

The measured intensities of the two CO bands were clearly related to the absolute CO concentrations that were measured in the product gas. For most of the spectra obtained with the nickel-based catalysts in the discharge, the CO signals were lower at the inlet side than at the outlet side. For the raw foam, this difference was much smaller. Furthermore, the inlet signal of the catalyst foams was below that of the raw foam signal, while it was higher at the outlet. This is an indication that oxidation of CO back to CO_2 , as was described for the CO_2 decomposition experiments in one of our former publications,⁶ is favored at the inlet of the reaction zone. Later on, at the outlet side, the concentration of other species that can be oxidized is higher and CO oxidation is retarded.

Unfortunately, this trend that was observed for most of the measurements, was not consistent through all spectra. Since the observed peaks were related to total product concentrations, the problems with the reactor regarding lowered yields by parasite discharges, as described above, often minimized the differences between the CO peaks in different spectra.

A consistent trend was observed for the CH C-X band at 314 nm. If the different catalysts were compared, the emission from CH increased in the following order: pure gas discharge < raw foam < nickel ≤ nickel/calcium. This trend is shown in Fig. 11 for two example curves.

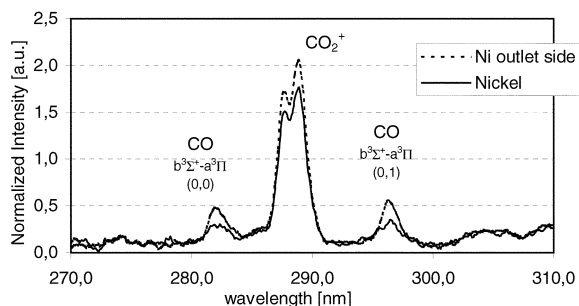


Fig. 9 CO_2 reforming of methane, CO emission, nickel catalyst, 40 °C.

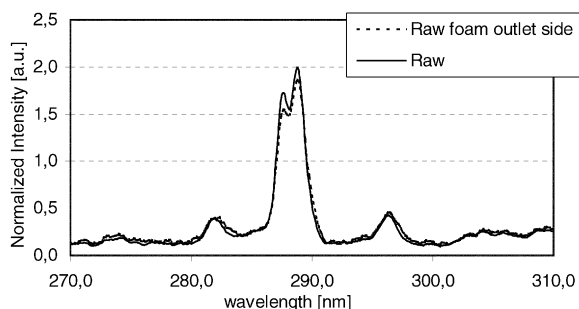


Fig. 10 CO_2 reforming of methane, CO emission, raw foam, 40 °C.

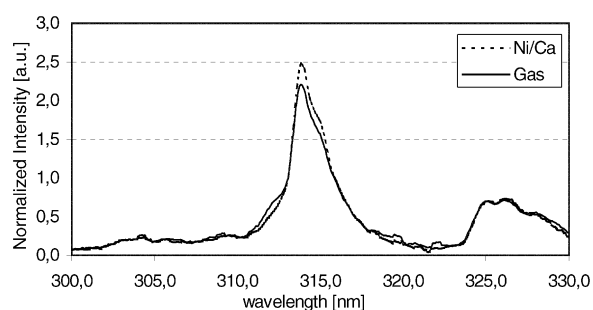


Fig. 11 CO_2 reforming of methane, CH C-X emission, pure gas discharge and nickel/calcium catalyst, 40 °C.

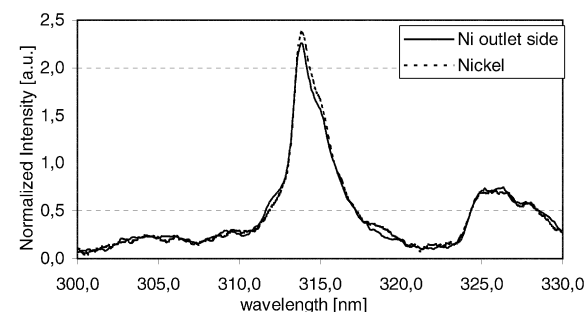


Fig. 12 CO_2 reforming of methane, CH C-X emission, nickel catalyst, 40 °C, comparison inlet/outlet of catalyst bed.

Besides the observation of higher CH signals with nickel catalysts, it was found that the signal was lower at the outlet side than on the inlet side of the catalyst bed, as shown in Fig. 12 for the nickel catalyst.

A higher gas temperature at the catalyst bed outlet, caused by the heat produced from the discharge could change the number of emitting CH radicals, either by acceleration of radical reactions that remove CH from the gas phase or a greater quantity of radiationless transitions.

Another conceivable interpretation could be that the consumption of CH increases during the passage through the catalyst bed or the production decreases due to other reaction pathways. If compared to the above-mentioned observation that CO signals were increasing from the inlet to the outlet of the catalyst bed, it could be a second hint that reactions of hydrocarbon species with oxygen are gaining importance towards the end of the catalyst bed.

As a last point in the analysis, the spectra obtained at different temperatures in CO_2 reforming of methane were compared. From all emission spectra, a similar trend for the CH C-X signal was observed. The normalized CH emission for the uncoated foam at 40, 160 and 300 °C is shown in Fig. 13.

Although the overall absolute emission intensity was rising, the height of the CH signal decreased significantly with respect

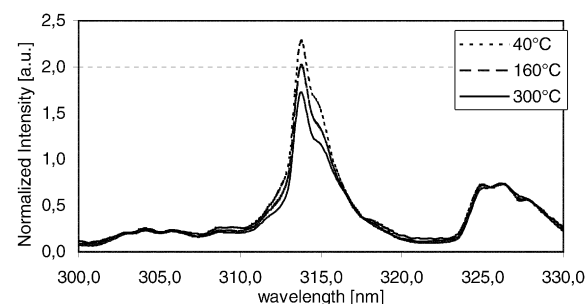


Fig. 13 CO_2 reforming of methane, CH C-X emission, uncoated foam, comparison of different temperatures.

to the CO₂ discharge bands with rising temperature. As explained above, this could be caused by a lower CH concentration at higher temperatures due to other reaction pathways and higher consumption rates or a change in the percentage of emitting CH radicals. Despite the overall decrease in emission intensity, the signal obtained with the nickel-based catalysts always remained stronger than that of the raw foam and the discharge-only experiment.

Conclusion

Although the observed differences in the emission spectra together with the results from numeric modeling can only be regarded as a first step towards the understanding of the plasma-catalyst interaction, we have tried to identify possible schemes for an interaction between the catalyst and the plasma. From the experiment with discharge and catalysts it was evident that a nickel-coated catalyst in the discharge plasma led to higher product yields in the reforming reaction. The synergetic effect between the catalyst and the discharge in the CO₂ reforming reaction could, in principle, be caused by two effects. First, the plasma properties could be influenced by the presence of a metal layer, which would be measurable as a change in the vibrational and rotational temperature of the discharge species, as was presented for example by Chen *et al.*²² and Suib *et al.*²³ An indication that such plasma-influencing effects of the nickel deposited on the support is not the main factor for the observed higher yields is found in the CH₄ decomposition with and without catalyst that was also presented in ref. 6. In these experiments, the yield of the main product hydrogen was nearly unchanged in the presence of catalyst. If an influence of the metal on the plasma properties were to be assumed, it should also be present in other reactions like CH₄ decomposition. Since this was not the case, an explanation based on the interaction between plasma species and the catalyst surface is more likely.

The identification of discharge species *via* optical emission spectroscopy showed that the relative intensity of the CH emission in the CO₂ reforming experiments was higher when a catalyst was present in the discharge gap. Furthermore, this intensity followed the activity trend of the catalysts that was also found by gas chromatography for the CO yield in the combined catalyst-discharge experiments (pure gas discharge < raw foam < nickel ≤ nickel/calcium), in the sense that the CH signal was higher for a more active catalyst.

This can be explained by either a lower consumption rate or a higher production rate for this molecule in the presence of a catalyst. If the production of CH is regarded as a pure plasma process, which is reasonable, the focus should be set on the consumption reactions. If conceivable reactions are taken from the kinetic modeling, there are two important reactions with high reaction rates:



Since no influence of the catalysts was observed in the CH₄ decomposition experiments, it is likely that oxygen-containing species are important for the promotional effects. Therefore, it can be assumed that the second reaction is more important. Following this idea, the catalyst surface would work as an acceptor for oxygen and oxygen-containing species like OH, such that the turnover of the gas phase reaction (eqn. (25)) is reduced, while at the same time the surface turnover of hydrocarbon species is enhanced. The path analysis for the production of carbon monoxide as the main product in the CO₂ reforming of methane showed that there is more than one important pathway leading to CO in the gas phase. Furthermore, when comparing the radical gas phase reactions with the catalytic

reaction schemes (as they were, for example, proposed by Bradford *et al.*²⁴), it is evident that there are several steps, which are found to be similar in the gas phase and in surface reactions.

Since an *in situ* investigation of the catalytic surface during plasma interaction was not part of the investigation, the formulation of an exact reaction mechanism for the interaction between the catalysts and the DBD plasma cannot be done at this stage. However, a tentative reaction scheme would definitely include the formation of hydrocarbon species on the catalyst surface by their direct adsorption from the gas phase or by adsorption of methane, followed by surface decomposition. Afterwards, these products would be gasified by oxygen-containing radicals from the plasma. As the concentration of surface oxygen species is enhanced on the catalyst surface in the presence of the discharge, the generation rate of carbon monoxide would be increased. Following this argumentation, the result from the CH₄ decomposition experiments that the use of a catalyst in the discharge did not increase the product yield would be the result of missing "consumption" reactions from hydrocarbon species on the surface.

Acknowledgements

The authors want to thank Eric Killer for his support of the experimental investigations.

References

- 1 B. Eliasson, U. Kogelschatz, B. Xue and L.-M. Zhou, *Ind. Eng. Chem. Res.*, 1998, **37**, 3350–3357.
- 2 U. Kogelschatz and B. Eliasson, in *Handbook of Electrostatic Processes*, ed. J.-S. Chang, A. J. Kelly and J. M. Crowley, Marcel Dekker, New York, 1995, pp. 581–605.
- 3 U. Kogelschatz and B. Eliasson, *J. Phys., Colloq.*, 1997, **7**, (C4), 47–66.
- 4 U. Kogelschatz, B. Eliasson and W. Egli, *Pure Appl. Chem.*, 1999, **71**, 1819–1828.
- 5 B. Eliasson and U. Kogelschatz, *IEEE Trans. Plasma Sci.*, 1991, **19**, 1063–1077.
- 6 M. Kraus, U. Kogelschatz, B. Eliasson and A. Wokaun, *Phys. Chem. Chem. Phys.*, 2001, **3**, 294–300.
- 7 T. C. Manley, *Trans. Electrochem. Soc.*, 1943, **84**, 83–96.
- 8 B. Eliasson, F. G. Simon and W. Egli, *Hydrogenation of CO₂ in a Silent Discharge*, in *Nonthermal Plasma Techniques for Pollution Control*, ed. B. M. Penetrante and S. E. Schultheis, NATO ASI Series G: Ecological Sciences, Springer, Berlin, 1993, vol. 34, part B, pp. 321–337.
- 9 B. Eliasson and U. Kogelschatz, *IEEE Trans. Plasma Sci.*, 1991, **19**, 309–323.
- 10 B. Eliasson, M. Hirth and U. Kogelschatz, *J. Phys. D*, 1987, **20**, 1421–1437.
- 11 B. Eliasson, W. Egli and U. Kogelschatz, *Pure Appl. Chem.*, 1994, **66**, 1275–1286.
- 12 M. Kraus, PhD Thesis, Swiss Federal Institute of Technology (ETH), Zurich, Switzerland, 2001.
- 13 W. Egli, KINETICS, ABB Corporate Research, Baden, Switzerland, 1991.
- 14 P. Deuffhard, *Num. Math.*, 1983, **41**, 373–398.
- 15 NIST Reference Database 17-2Q98: Chemical Kinetics, National Institute of Standards and Technology, Gaithersburg, MD, 1998.
- 16 W. Tsang and R. F. Hampson, *J. Phys. Chem. Ref. Data*, 1987, **16**, 471–508.
- 17 W. Tsang and R. F. Hampson, *J. Phys. Chem. Ref. Data*, 1986, **15**, 1087.
- 18 W. Tsang and R. F. Hampson, *J. Phys. Chem. Ref. Data*, 1988, **17**, 887.
- 19 W. Tsang, *J. Phys. Chem. Ref. Data*, 1990, **19**, 1–68.
- 20 W. Tsang, *J. Phys. Chem. Ref. Data*, 1991, **20**, 221–273.
- 21 R. W. B. Pearse and A. G. Gaydon, *The identification of molecular spectra*, Chapman & Hall, London, 1965.
- 22 X. Chen, M. Marquez, J. Rozak, C. Marun, J. Luo, S. L. Suib, Y. Hayashi and H. Matsumoto, *J. Catal.*, 1998, **178**, 372–377.
- 23 S. L. Suib, S. L. Brock, M. Marquez, J. Luo, H. Matsumoto and Y. Hayashi, *J. Phys. Chem., B*, 1998, **102**, 9661–9666.
- 24 M. C. J. Bradford and M. A. Vannice, *Catal. Rev.-Sci. Eng.*, 2000, **41**, 1–42.